N configuration control of N-doped carbon for stabilizing Cu nanoparticles: The synergistic effects on oxy-carbonylation of methanol

Jinping Zhang, Xiaoying Liu, Weikun Chen, Huihuang Fang, Yanping Zheng, Youzhu Yuan[*]

State Key Laboratory of Physical Chemistry of Solid Surfaces, National Engineering Laboratory for Green Chemical Productions of Alcohols—Ethers—Esters, iChEM, College of Chemistry and Chemical Engineering, Xiamen University, Xiamen, 361005, China

A R T I C L E   I N F O

A B S T R A C T

N-doped carbons (NCs) have attracted considerable attention for their outstanding physicochemical properties, including tunable porosity, electronic features and modified surface. Here, we report the preparation of hierarchically porous NCs derived from the direct pyrolysis of ZIFs (ZIF-7 and ZIF-8) and poly—m—phenylenediamine-covered carbon black (PmPDA-C) for the stabilization of Cu nanoparticles (NPs). The configuration of N species can be effectively regulated by changing the ligand of ZIFs and pyrolysis atmosphere. A remarkable N configuration synergistic effect is observed in the oxy-carbonylation of methanol to dimethyl carbonate with molecular oxygen. The results indicate that the Cu NPs on pristine carbon have a turn over frequency (TOF) of 4.4 h^{-1} for the reaction, while those on NCs from ZIF-8 and ZIF-7 present TOF values as high as 17.9 h^{-1} and 28.5 h^{-1}, respectively. The extensive characterizations reveal that NCs with a nitrogen content of 2—5 wt% and a pyrrolic-/pyridinic-N molar ratio of 2—3 are vital for the performance enhancement of Cu NPs. This work shows that the stabilization and enhanced performance of active Cu NPs on NCs are realized by the rational design of precursors to generate the proper N configurations.

© 2019 Elsevier Ltd. All rights reserved.

1. Introduction

Carbon-based materials have been viewed as one of the most important catalysts or catalyst supports in many practical applications, such as electrochemistry [1—6], drug delivery [7—10], gas capture and separation [11—13], catalysis including oxidation and hydrogenation [14—19], and oxy-carbonylation [20—23]. However, pristine carbon materials are relatively chemically inert to anchor an active metallic phase because of insufficient bonding sites on the surfaces, leading to inferior dispersion and stability of the metal nanoparticles. Active carbon-based materials with functionalized surfaces, tunable porosity and electronic properties are desperately needed. Many efforts have been made to fabricate functionalized carbon materials with heteroatoms, such as N, B, P, and S. The introduced heteroatoms can alter the charge distribution of a carbon surface and expand the potential applications. The N heteroatom has been most extensively studied among the various dopants because the similar atomic radius of N and C does not result in lattice mismatch after the incorporation of N into carbon supports.

There are many works on either the preparation method or catalytic impact of N-doped carbon materials (NCs). In particular, NCs have been used for stabilizing metal active species in different heterogeneous catalytic reaction systems [24—26]. Usually, NCs can be obtained by chemical vapor deposition [27,28], laser ablation [29,30], and carbonization of N-containing polymers [31,32]. These methods can only prepare randomly N-doped carbon materials after multistep reaction processes without precisely controlling the type and concentration of N, which retards understanding the structural nature of the catalysts. Insight into the role of N in NCs is mostly reported in ORR systems. For example, Nakamura group showed that pyridinic N species are the active sites for the ORR in acidic media [33]. Yu group reported that the ORR activity corresponded with the ratio of pyridinic N to graphitic N in NCs under alkaline conditions [34]. However, for heterogeneous catalysis reaction systems, relevant studies are rare and unclear.

Taking the oxy-carbonylation of methanol reaction system as an example, Cu-based catalysts supported on carbon materials have been widely studied. Li group proved that Cu-based catalysts supported on a certain concentration of nitric acid-treated activated

carbon (AC) exhibited optimal catalytic activity with 12 nm Cu particles [22]. Cu@HCS (HCS represents hollow carbon spheres) showed highest methanol conversion with 2 nm Cu particles and 200 nm carbon spheres [23]. During these studies, the regulation of Cu particles had been the focus of research by modifying the surface structure of pristine carbon support to improve the catalytic performance. Recently, there were some reports about the use of NCs to control the dispersion of Cu species and improve the yield of dimethyl carbonate (DMC) in the reaction. For example, Cu/NCNTs (NCNTs: N-doped carbon nanotubes) catalysts had highest yield of DMC when the size of Cu species was 2.6 nm. The Cu dispersion increased with increasing the N content from 0 to 5.9 wt%. The N content was affected by the O–containing groups of carbon material [35]. Ren and Li groups reported Cu@NHCS (NHCS represents N-doped hollow carbon spheres) had the highest TOF value (11.0 h^{-1}) with 7.4 nm Cu particles and 4.0 wt% N content. The DMC yield decreased with further increasing the N content to 5.4 wt%. The effective N species were simply considered to be pyridinic and graphitic N [20]. Cu/NG (NG: N-doped graphene) had highest catalytic performance when the N content was as high as 7.6 wt% with 7.5 nm Cu particles [21]. Nevertheless, the N content in most of literature was all below 10 wt% with ambiguous understanding on the effects of N configuration, and the effect of O containing group was difficult to exclude. Until now, the reports on the effects of different N species on structure and performance of active metal species through a rational systematical regulation of N configuration are sporadic. The difficulties of research lie in the blending and inhomogeneity of different N types in NCs, mainly including pyrrolic, pyridinic and graphitic N. Therefore, it is highly demanded to further investigate the regularity among N species, Cu species and catalytic performance by using a rational method to prepare NCs coupled with a series of characterizations.

Metal-organic frameworks (MOFs), consisting of metal ions and organic ligands, have been proven to be feasible sacrificial templates to fabricate various functionalized carbon-based materials [4,15,36–41]. Among them, zeolitic imidazolate frameworks (ZIFs), a subfamily of MOFs, are ideal candidates to fabricate NCs with high N content and thermal stability via facile synthesis by controllable pyrolysis [42,43]. These N-rich MOFs have the potential to generate structural integrity and high electrical conductivity of NCs to facilitate electron transfer and enhance catalytic activity [2,15,44]. Many NCs derived from MOFs have been widely applied in electrochemical reactions [2,45–48], sensing and gas adsorption [49–51] with outstanding performances. However, few studies have focused on these NCs supported catalysts in gas-liquid catalysis due to the complex reaction process and low yield of NCs, which increase the difficulty of investigating the structure-performance correlations. As far as we know, there is no report on the use of NCs derived from ZIFs as supports for the oxidative carbonylation of methanol to DMC.

In this work, we report a method for efficiently producing NCs using ZIFs (ZIF-7 and ZIF-8) as platforms with adjustable N species and concentration in the range of 0–20 wt%. Additionally, a series of NCs-supported Cu NPs are prepared and employed for the oxy-carbonylation of methanol to DMC with highly dispersed Cu species before and after the reaction. This work aimed to investigate the relationship among N configurations, Cu species and catalytic performance for a reaction.

2. Experimental

2.1. Catalyst preparation

2.1.1. Synthesis of ZIF-8

The ZIF-8 nanocrystals were prepared by following a modified procedure reported in the literature [52,53]. Typically, 2.790 g of Zn(NO$_3$)$_2$·6H$_2$O and 3.080 g of 2-methylimidazole (MeIM) were dissolved in 75 mL methanol to create a homogeneous solution at room temperature. The Zn(NO$_3$)$_2$·6H$_2$O methanol solution was dropped into the 2-methylimidazole (MeIM) methanol solution under vigorous stirring. Then, the ZIF-8 nanocrystals were grown at 35 °C under static conditions for 24 h. The as-prepared precipitates were separated by centrifugation, washed with methanol three times and then dried in air at 100 °C overnight.

2.1.2. Synthesis of ZIF-7

The ZIF-7 nanocrystals were synthesized by following reported procedures [54]. Typically, 2.720 g Zn(NO$_3$)$_2$·6H$_2$O was dissolved in 100 mL N,N-dimethylformamide (DMF), which was added into 100 mL methanol containing 2.400 g benzimidazole (PhIM) under vigorous stirring for 3 h at room temperature. Then, the above mixture was centrifuged and washed with copious amounts of methanol. Finally, white ZIF-7 was dried at 100 °C overnight.

2.1.3. Synthesis of PmPDA-C

Commercial carbon black (C) was treated in HNO$_3$ at 100 °C for 16 h. The PmPDA-C precursors were prepared using a modified method according to the previous literature [18]. Briefly, m-phenylenediamine (3.0 g) and carbon black (0.4 g) were dispersed and stirred in a concentrated HCl aqueous solution under ice water bath conditions. Then, precooled (NH$_4$)$_2$S$_2$O$_8$ (2.0 M, 28 mL) was dropped slowly into the suspension to oxidize m-phenylenediamine. After a period of 24 h for stirring, the suspension solution was filtered and washed with deionized water until the filtrate was neutral. Then, the sample was dried at 100 °C overnight to obtain the N-doped carbon material, which was named PmPDA-C.

2.1.4. Preparation of NCs from ZIFs and PmPDA-C

The porous NCs were fabricated using ZIFs (ZIF-7 and ZIF-8) as self-sacrificed templates by calcining at different temperatures (700 °C, 800 °C, 900 °C, 1000 °C and 1100 °C) with a rate of 2 °C/min under an Ar atmosphere for 4 h. Next, the as-synthesized samples were immersed in HCl (3 M, 100 mL) at room temperature for 24 h to remove the metal Zn component. Subsequently, the samples were isolated by filtration and washed with deionized water until the pH of the filtrate was neutral before drying at 100 °C overnight. Similarly, the NCs from PmPDA-C precursor were also obtained by directly pyrolysis in an Ar atmosphere without HCl washing. The obtained materials from ZIF-8, ZIF-7 and PmPDA-C are abbreviated as NCs-T, NCs-T* and NCs–P-T, where T indicates the calcination temperature of the precursors, and P means polymerization.

2.1.5. Construction of NCs with controllable N species and content

To explore and regulate the N species in the NCs, a strategy was adopted by using high-temperature steam to selectively etch carbon species and thus to control the N type and content in the NCs. In a typical procedure, taking NCs-900 as an example, after the ZIF-8 nanocrystals were heated to 900 °C at the rate of 2 °C/min under an Ar atmosphere for a certain time, the Ar flow was switched to go through an ultrapure water tank to obtain a water-steam containing atmosphere for pyrolysis. The whole pyrolysis time was 4 h. The steam-treated carbon materials were denoted as NCs-900-t (t means the time of the steam treatment).

2.1.6. Preparation of Cu-based catalysts supported on NCs

The supported Cu catalysts were then obtained by using different NCs and commercial active carbon (XC72) as carriers and copper salts as the precursor through a conventional impregnation method. The theoretical Cu loading was set as 2.0 wt%, 4.0 wt%, 6.0 wt%, 8.0 wt% and 10.0 wt%. Typically, the supports were added

into the copper solution and ultrasonically treated for 30 min. Then, the muddy mixture was held under static conditions for 5 h to guarantee impregnation balance and then stirred until solvent evaporation at 70 °C. The as-obtained catalyst precursors were dried at 100 °C overnight and treated in an Ar atmosphere at 400 °C for 2 h at a rate of 2 °C/min. The prepared catalysts were labeled as Cu/NCs-*T*, Cu/NCs-900-t, Cu/NCs-*T**, Cu/NCs—P-*T*, and Cu/XC72.

2.2. Catalyst characterization

Powder X-ray diffraction (XRD) patterns were recorded on a Rigaku IV diffractometer, equipped with graphite mono-chromatized Cu—K_α radiation ($\lambda = 1.5418$ Å) as the X-ray source. The scanning speed was set as 10°/min from 4° to 90°. MDI Jade 6.5 software was used to process and assign the diffraction peaks.

The Raman spectra were collected using a 532 nm excitation by a 13 mW He—Cd laser source on a Renishaw Invia Raman microscope with the CCD detector. The exposure time was 10 s.

The specific surface area and porous properties of the catalysts were measured by N_2 adsorption/desorption isotherms at 77 K on the Micromeritics ASAP 2020 instrument. Before the analysis, the catalysts were pretreated under vacuum at 100 °C for 5 h. The Brunauer-Emmett-Teller (BET) method was used to calculate the specific surface area of the samples (S_{BET}). The mesoporous surface area (S_{meso}) was evaluated by the *t*-plot and Barret-Joyner-Halenda (BJH) methods.

Transmission electron microscopy (TEM) was performed to observe the morphological structure of samples on a Phillips Analytical FEI TECNAI F20 electron microscope with a 300 kV electron acceleration voltage. The STEM system was chosen to investigate the element dispersion of the catalysts in the dark field. The samples were dispersed in ethanol under ultrasound and then dropped onto a copper TEM grid.

H_2—temperature programmed reduction (H_2—TPR) measurements were recorded using a Micromeritics AutoChem II 2920 instrument with a thermal conductivity detector (TCD). Fifty milligrams of catalyst was loaded into the U-shaped quartz tube and pretreated at 150 °C for 3 h at 30 mL/min N_2 atmosphere. Then the gas was switched to 5 vol% H_2/Ar after cooling to 50 °C. The H_2—TPR curves were recorded by the TCD from 50 to 900 °C with a heating rate of 10 °C/min.

Inductively coupled plasma mass spectrometry (ICP-MS) was used to determine the actual Cu content in catalysts on an Agilent ICP-MS 4500 instrument. Thermo—gravimetric analysis (TGA) was conducted on a TA209F1 analyzer with a ramp rate of 10 °C/min under air atmosphere to explore the interactions between Cu and NCs. Element analysis was measured to detect the N content on a Vario EL III analytical instrument. Electrochemical impedance spectroscopy (EIS) was performed to investigate the electron transfer between metal species and supports in catalysts using a CHI660E electrochemical station.

X-ray photoelectron spectroscopy (XPS) was carried out on a Qtac-100 LEISS spectrometer with a 300 W monochromatic Al—K_α excitation source. The binding energies of the catalysts were corrected according to the C1s peak at 284.6 eV.

2.3. Catalytic reaction

The oxy-carbonylation of methanol was evaluated in a fixed-bed reactor—gas chromatograph (GC) combined system. For each catalytic evaluation, 100 mg catalyst mixed with 400 mg of quartz grains was loaded into a quartz tubular reactor with a 7 mm inner diameter. Methanol vapor, which was supplied from a bubbling generator at 283 K, was introduced by the gas mixture of CO (26 mL/min) and O_2 (2 mL/min) into the catalyst bed with the

defined reaction temperature. The reaction pressure was set as 1.0 MPa. The hot gas products were collected by an online six-way valve (DC6UWT) and detected by using an online gas chromatograph (GC-2060, Shanghai, China). Methanol, DMC and the byproducts dimethyl ether (DME), methyl formate (MF) and dimethoxymethane (DMM) were analyzed with a flame ionization detector (FID) and a capillary column (KB-WAX, 60 m $\times$ 0.32 mm $\times$ 0.33 μm).

The conversion of methanol (C_{MeOH}), DMC selectivity (S_{DMC}), and turnover frequency (TOF) were determined as follows:

$$C_{MeOH} = \frac{Moles\ of\ methanol\ converted}{Total\ moles\ of\ methanol}$$

$$S_{DMC} = \frac{2 \times Moles\ of\ DMC\ produced}{Moles\ of\ methanol\ converted}$$

$$TOF = \frac{Moles\ of\ methanol\ converted}{Cu\ atoms \times Time}$$

3. Results and discussion

3.1. Structure and morphology of catalysts

The porous NCs and Cu-based catalysts were successfully prepared by thermolysis and postimpregnation steps. For example, Fig. 1 displays the preparation of Cu/NCs-*T*. The synthetic process can fully utilize the textural advantages of the ZIF-8 to obtain a high N content. Moreover, the N configuration and doping level can be adjusted effectively by controlling the pyrolysis temperature or modifying the organic ligand in the ZIF-8. The structures of ZIFs nanocrystals, NCs and supported Cu-based catalysts were characterized by XRD (Fig. 2 and S1). The diffraction peaks of ZIFs (Fig. S1a) are consistent with those reported in literature [46,53], illustrating the successful preparation of ZIFs with specific structures. The XRD patterns of NCs-*T* and corresponding Cu/NCs-*T*
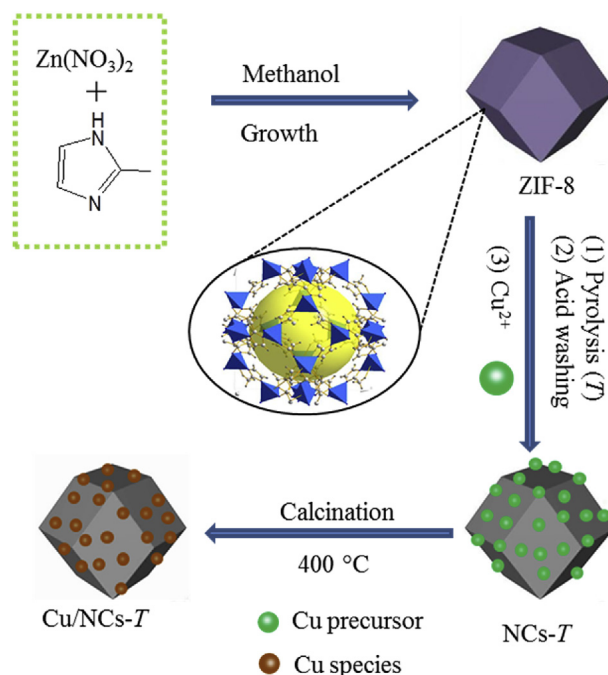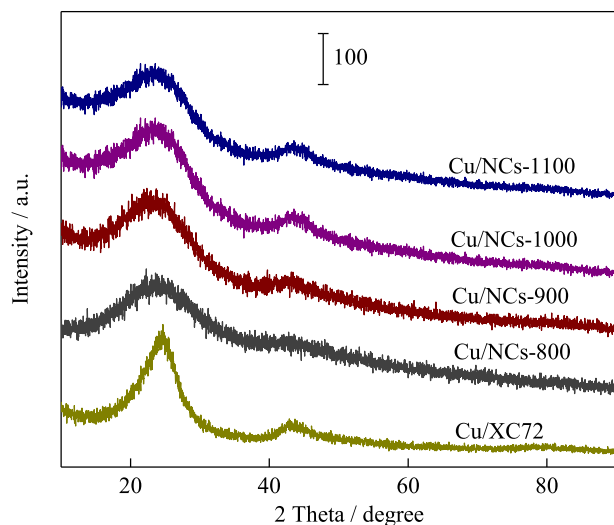

Fig. 1. Schematic illustration of the synthetic route for NCs-*T* and Cu/NCs-*T*.

Fig. 2. Powder XRD patterns of Cu/NCs-T and Cu/XC72 catalysts with 4 wt% Cu loading. (A colour version of this figure can be viewed online.)

catalysts are drawn together under the same scale. The NCs-T from ZIFs exhibited similar diffraction peaks as the pure carbon XC72 (Fig. S1b). They all had one broad peak at approximately 24.0°, which corresponds to the (002) diffraction of graphitic NCs, indicating a disordered carbon structure and imperfect crystallinity [21,31]. The diffraction peak at approximately 44 °C, attributed to the (100) plane of NCs, was slightly enhanced with increasing pyrolysis temperature whether for NCs-T or Cu/NCs-T (Figs. S1b and 2). This change implied that small-scale graphene sheets were formed and the graphitization of NCs increased [55–57]. The tendency is not significant especially for NCs-T obtained at relatively low temperatures. However, the following characterizations by Raman and XPS proved that the graphitization of NCs-T was promoted with increasing pyrolysis temperature. The XRD patterns in Fig. 2 indicated that no diffraction peaks were assigned to Cu-containing crystalline phases, which suggested that there were no large Cu particles in Cu/NCs-T catalysts.

The C configuration was investigated by Raman. As shown in Fig. S2a the NCs-T supports exhibited two characteristic peaks located at round 1340 cm^{-1} (D band) and 1590 cm^{-1} (G band), which implied the defect level in graphitic structure and the in-plane vibration of graphitic sp^2 carbon in supports [58]. The integrated intensity ratio of the D band and G band (I_D/I_G) reflects the structure defect of carbon material [18]. The plot of I_D/I_G values of NCs-T as a function of pyrolysis temperature is shown in Fig. S2b. The I_D/I_G value decreased gradually when the pyrolysis temperature rose from 800 °C to 1100 °C, indicating that it was more favorable to promote the graphitization of NCs-T supports than create more defect sites by increasing the pyrolysis temperature. This results are consistent with the reports in literature [59]. Combined with the following the experimental results, it was found that the graphitization of C configuration had a positive effect on the catalytic activity.

The specific surface area and porosity of the ZIF-8 nanocrystals, NCs-T supports and Cu/NCs-T catalysts were investigated by N$_2$ adsorption/desorption measurements (Fig. S3 and Table S1). The I-type isotherms and hysteresis loop of NCs-T and Cu/NCs-T proved their micro/mesoporous structures from the inheritance of the ZIF-8 texture and Zn evaporation during the calcination process [1]. The S_{BET} and S_{meso} of NCs-T increased with the pyrolysis temperature increasing from 800 °C to 1000 °C, indicating that the evaporation of Zn facilitated the generation of mesopores. When the

temperature increased to 1100 °C, the surface area of NCs-1100 decreased due to the increase in the graphitic and stacking degrees [1]. After Cu loading, the S_{BET} and S_{meso} of Cu/NCs-T increased further. The presence of mesopores guarantees efficient mass transport and facilitates the promotion of catalytic activity [4,45]. However, the following catalytic results proved that the activity would not depend on the increase in the surface area.

TEM and HAADF-STEM images were taken further to observe the morphology and structure information as shown in Fig. 3. It can be seen that the geometric structures of ZIF-8 nanocrystals were typical of a polyhedral morphology, similar to the results reported previously [4,60]. NCs-T samples maintained structural integrity and high dispersion with slightly crumpled surfaces due to high-temperature calcination (Fig. 3b and c). For Cu/NCs-900 and Cu/NCs-1000 catalysts, Cu species were highly dispersed on the NCs-T supports, and no significant agglomeration was observed in Fig. 3d and e. Moreover, no obvious Cu species were observed in the bright-field images of Cu/XC72, which might be covered by an overlapping carbon layer. The results are coincided with the analysis results of the corresponding XRD patterns. The STEM mapping further verified that the Cu species were relatively uniformly dispersed on the NCs-T supports (Fig. 3g). The TGA results of Cu/XC72, Cu/NCs-1000 and Cu/NCs-1100 are shown in Fig. S4. These samples consisted of 4 wt% Cu and 96 wt% support including carbon and nitrogen species. As for Cu/NCs-800 and Cu/NCs-900, after air treatment from 35 °C to 1000 °C, the weight loss was approximately 84 wt% and 90 wt%, respectively. Considering the fact of much higher N content in NCs-800 than NCs-900 (Table 2), the finding implied that Cu species should have a strong interaction with N in NCs-T.

3.2. Catalytic performance

The oxy-carbonylation of methanol to DMC was carried out over a series of Cu/NCs-T catalysts. The effects of Cu loadings and ZIF-8 pyrolysis temperatures on catalytic activity were systematically investigated. The catalytic activity could be improved to some extent by increasing the loading of Cu, as shown in Fig. S5. The conversion of methanol was only 6.5% with 92.3% DMC selectivity when the Cu loading was 2 wt%. Increasing Cu loading to 4 wt%, the methanol conversion and DMC selectivity increased to 41% and 97.3%, respectively. The conversion of methanol was further improved with 6 wt% Cu loading. Then, the methanol conversion remained almost constant, even with increasing the Cu loading to 10 wt%. Based on these experimental results, we chose the catalysts with 4 wt% Cu loading for further investigations.

Fig. 4a shows that the conversion of methanol increased with increasing ZIF-8 pyrolysis temperature for a series of Cu/NCs-T catalysts. Simultaneously, the DMC selectivity was retained above 95% for pyrolysis temperatures ranging from 950 to 1100 °C. Cu/NCs-1000 and Cu/NCs-1100 both showed higher catalytic activity than Cu/XC72. Moreover, taking Cu/NCs-900 and Cu/NCs-1000 as examples, there is a large gap in the catalytic activity. For Cu/NCs-900, the methanol conversion was lower than 5% with 82.3% selectivity to DMC. However, the Cu/NCs-1000 exhibited better catalytic performance with 40% methanol conversion and 97.3% DMC selectivity. This change indicated that the N configuration and amount have a great influence on the catalytic activity.

A series of experiments were carried out by altering the pyrolysis atmosphere or organic ligand in the ZIF-8 synthesis process to investigate the role of N configuration. Fig. 4b displays the performance of Cu/NCs-900-t catalysts, which showed higher catalytic activity than Cu/NCs-900 (Fig. 4a). After steam treatment for 1 h, the catalytic activity increased slightly. Upon extending the steam-treated time to 2 h, the conversion of methanol further increased with 91.1% DMC selectivity. When prolonging the treatment time to
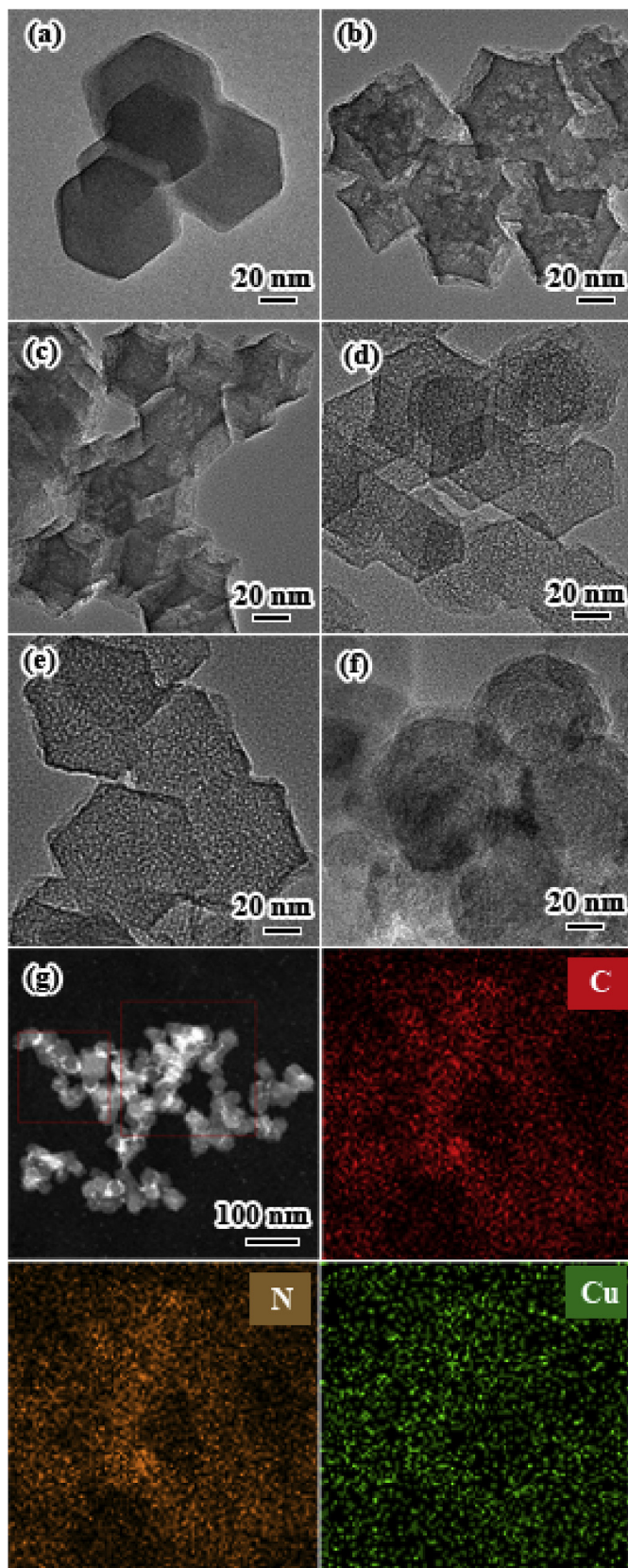
Fig. 3. TEM images of (a) ZIF-8, (b) NCs-900, (c) NCs-1000, (d) 4 wt% Cu/NCs-900, (e) 4 wt% Cu/NCs-1000, and (f) 4 wt% Cu/XC72; STEM image of (g) 4 wt% Cu/NCs-1000 for elemental mappings of C, N, and Cu in the red rectangle of (g).

3 h, Cu/NCs-900-3 h showed the highest catalytic activity with 32.7% conversion of methanol and 97.3% selectivity to DMC. When continuing to extend the steam-treatment time, the methanol conversion declined to 28% but the selectivity to DMC remained above 95%.

On the other hand, ZIF-7 nanocrystals were also prepared as precursors by using benzimidazole instead of 2-methylimidazole to tailor the N species in catalysts. Cu/NCs-900* from ZIF-7 nano-crystals displayed better catalytic activity than Cu/NCs-900 (35% methanol conversion and 97.6% DMC selectivity). Compared with Cu/NCs-1000, the methanol conversion for Cu/NCs-1000* was increased by more than 20% with high selectivity to DMC (98.5%). The activity was similar to that of the Cu/NCs-1100 catalyst. When the pyrolysis temperature increased to 1100 °C, the conversion of methanol and DMC selectivity remained above 60% and 98%, respectively. These results demonstrated that the structure of the NCs-*T* supports was closely related to the catalytic activity. It is very important to explore the differences among the NCs-*T* supports.

The TOF values based on total Cu atoms were calculated to further probe the intrinsic activity of catalysts with methanol conversion below 20%. The results are summarized in Table 1. The Cu/NCs-700, Cu/NCs-800 and Cu/NCs-900 catalysts showed low TOF values. The TOF values over Cu/NCs-1000 and Cu/NCs-1000* were 17.9 h^{-1} and 28.5 h^{-1}, respectively, which were 4–6 times higher than that of Cu/XC72. Because the total Cu content was around 4.0 wt% as determined by ICP-MS, the difference in TOF values might be mainly attributed to the variation of N species. Moreover, compared with the other N doped carbon supported Cu-based catalysts reported in literature, Cu/NCs-1000 and Cu/NCs-1000* showed better performance with higher TOF values even if the data were calculated based on total Cu content.

3.3. Relationship between catalytic performance and the structure of N species in NCs

The intrinsic activity of catalysts is usually related to the surface structure of catalysts, the electronic transfer and the synergistic effect between the supports and metal sites. In our work, because the Cu loading in the catalyst was similar, we mainly examined the surface structure of the supports and electronic interactions with Cu species.

The N content of the Cu/NCs-*T* catalysts was measured by elemental analysis as shown in Table 2. This analysis indicated that the N content in the Cu/NCs-*T* samples gradually decreased from 18.4 wt% to 2.0 wt% with increasing pyrolysis temperature. Corre-spondingly, the molar ratio of N/Cu declined from 22.9 to 2.2. Combined with the catalytic performance, the methanol conver-sion rate was promoted rapidly when the molar ratio of N/Cu was less than 5.1. To study the role of N, an experiment was designed by increasing the Cu loading to 8 wt% on NCs-900. The molar ratio of N/Cu in 8 wt% Cu/NCs-900 decreased to approximately 5.5, similar to that of 4 wt% Cu/NCs-1000 (Table S2). The conversion of meth-anol changed in the following order: 4 wt% Cu/NCs-1000 > 8 wt% Cu/NCs-900 > 4 wt% Cu/NCs-900 (Fig. S6). For 4 wt% Cu/NCs-900 and 8 wt% Cu/NCs-900, the methanol conversion could be improved by increasing the Cu loading to some extent. Comparing 8 wt% Cu/NCs-900 and 4 wt% Cu/NCs-1000, the variation in methanol conversion might be attributed to the influence of the N species in the catalysts because they have similar N/Cu molar ratios. It can be speculated that the structure and amount of N have important effects on the catalytic performance.

To control the N species in Cu/NCs-*T* catalysts, two strategies were adopted: (1) introducing water-steam into the pyrolysis process to selectively etch carbon species; (2) choosing a similar ligand instead of 2-methylimidazole to prepare ZIF-7 nanocrystals.

Table 1
The catalytic performance for DMC synthesis on a series of Cu-based catalysts.

Catalyst	Mass/mg	Cu[a]/wt%	Methanol conv./mol%	DMC selec./mol%	TOF/h^{-1}
Cu/NCs-700	100	4.3	1.5[b]	47.1	0.13
Cu/NCs-800	100	4.4	2.6[b]	64.9	0.23
Cu/NCs-900	100	4.2	3.7[b]	82.3	0.34
Cu/NCs-1000	10	4.2	19.6[b]	98.3	17.9
Cu/NCs-1000*	10	4.0	19.3[c]	98.5	28.5
Cu/XC72	10	3.9	4.5[b]	96.8	4.4
Cu/NHCS [20]	100	9.8	2.1	96.6	11.0
Cu/NCNTs [35]	300	8.0	2.4	97.8	17.6
Cu/NG [21]	100	7.0	3.1	97.6	16.9

Reaction conditions: $T = 110\ °C$, $P = 1.0$ MPa, CH$_3$OH = 0.8 mol% [b], CH$_3$OH = 1.2 mol% [c].
[a] Obtained by ICP-MS.

Table 2
Element analysis of Cu/NCs-T catalysts.

| Catalyst	N/Cu[a]/molar ratio	C/N	Content/wt%		
			N	C	H
Cu/NCs-1100	2.2	36.3	2.0	72.5	2.0
Cu/NCs-1000	5.1	15.0	4.8	72.0	2.3
Cu/NCs-950	7.6	12.9	6.4	82.7	3.6
Cu/NCs-900	11.4	6.3	9.8	62	2.0
Cu/NCs-800	15.2	3.1	15.8	48.9	3.0
Cu/NCs-700	22.9	2.3	18.4	41.4	3.4

[a] The Cu content was determined by ICP-MS.

The catalytic activity over Cu/NCs-900-t and Cu/NCs-T* has been discussed above (Fig. 4b). The N content in these catalysts is explored in Table S2. For Cu/NCs-900-t catalysts, the results proved that the N content decreased with increasing steam treatment time, while the catalytic performance was promoted. After steam treatment for 2 h, the N content in Cu/NCs-900-2 h declined to 7.4 wt%, and the conversion of methanol only increased by 3.8%. When the N content decreased to 4.0−5.0 wt%, the catalytic activity was sharply promoted, which proved that the N content had a significant influence on the catalytic performance. Based on the above experimental results, we found that the NCs-supported Cu catalysts with similar Cu loading could show higher activities when the N content was 2−5 wt% (Table 2 and S2). Moreover, comparing Cu/NCs-900*, Cu/NCs-900-3 h and Cu/NCs-1000 show they have different methanol conversion, although they have similar N contents. The methanol conversion on Cu/NCs-1000* was approximately 25% higher than that on Cu/NCs-1000, and the N content in both catalysts differed by only approximately 2%. The results showed that the catalytic performance was also related to the structure of N species in the NCs-T supports.

XPS is a valid technique to discriminate the different N species of NC supports. Fig. 5a shows the N 1s XPS profiles of the three NCs-T supports. The N species were mainly deconvoluted into three peaks in the form of pyridinic N (N1), pyrrolic N (N2), and graphitic N (N3) [1,4,61,62]. Fig. 5b displays the concentration distribution of the three N species in NCs-T as a function of pyrolysis temperature. The concentration of N1 decreased with increasing pyrolysis temperature. In terms of NCs-900, the N species were dominated by N1 species (50.8%) and contained 40.3% N2 structure. Compared with that in NCs-900, the N1 concentrations in NCs-1000 and NCs-1100 decreased to 38.6% and 26.7%, respectively, while the N2 species increased to 51.5% and 58.6%, respectively. Simultaneously, the N3 species also slightly increased. The finding indicates that increase of pyrolysis temperature could promote the formation of N2 and N3 species. The change trend of the N species agrees with the literature results [25,48,63]. Interestingly, in a similar report by Song et al. [31], the concentration of N2 species declined up to 600 °C. The different experimental results proved that the stability of N species
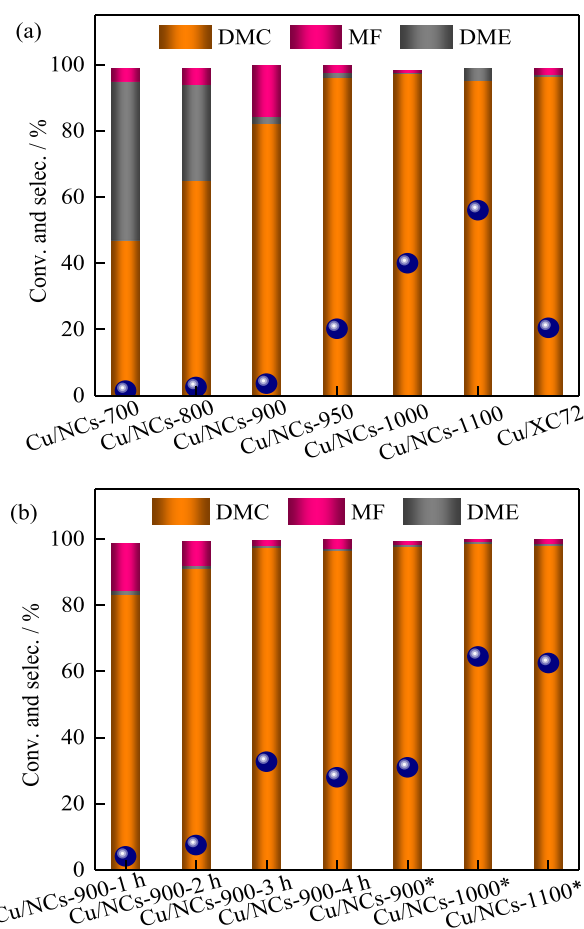
Fig. 4. Catalytic activity over (a) 4 wt% Cu/NCs-T from ZIF-8 and 4 wt% Cu/XC72, and (b) 4 wt% Cu/NCs-T-t from ZIF-8 and 4 wt% Cu/NCs-T* from ZIF-7. Reaction conditions: 0.1 g catalyst, $T = 110\ °C$, t = 8 h, $P = 1.0$ MPa, WHSV = 16800 mL/g/h, CH$_3$OH = 0.8 mol%.

could be affected by the small differences in the properties and treatment conditions of the precursors. To further explore the effects of pyrolysis temperature on NCs-T supports, we conducted the measurements of C1s and O1s XPS, which are shown in Fig. S7. The C1s peaks were deconvoluted with three different components located at 284.6 ± 0.1 eV, 285.6 ± 0.1 eV and 286.6 ± 0.1 eV, which belonged to sp^2 hybridized C=C, C==N and sp^3 structural C−N respectively [59,64]. The concentration of different C species was listed in Table S3. With increasing pyrolysis temperature, the concentration of sp^2 hybridized carbon species (C=C and C=N) increased while that of sp^3 carbon (C−N) decreased. This reflected
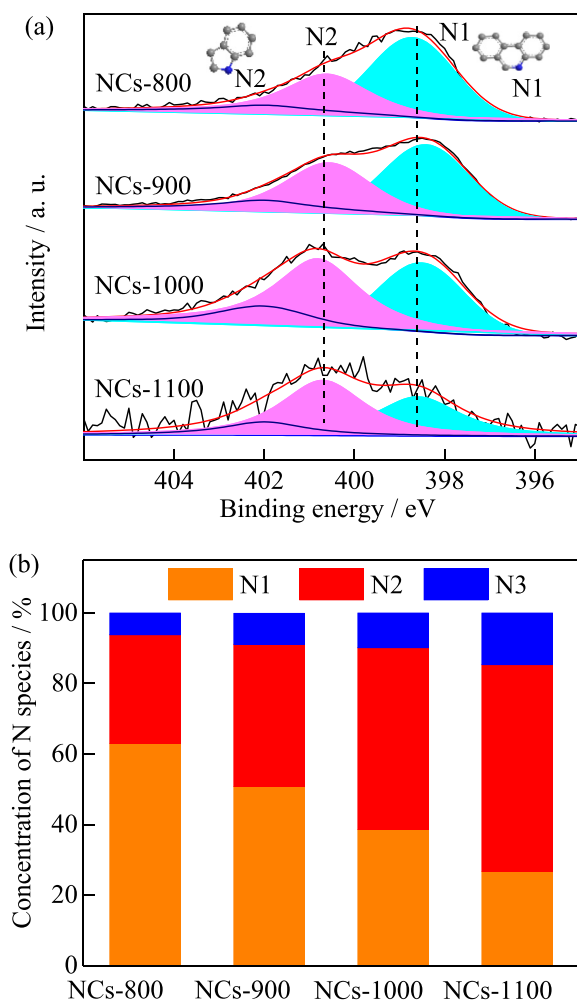
Fig. 5. N 1s XPS profiles of (a) NCs-*T* supports and (b) concentration of different N species including pyridinic N (N1), pyrrolic N (N2), and graphitic N (N3).

the higher pyrolysis temperature promote graphitization of NCs-*T*, which could effectively enhance the electron transfer [65]. The results corresponded with the Raman spectra and TEM images. The O 1s spectra are typically fitted into two components associated with singly and doubly bonded O atoms at 532.5 ± 0.1 eV and 531.2 ± 0.1 eV respectively [66]. Singly bonded O atoms may mainly be present as hydroxyl groups (C—OH), while doubly bonded O atoms may be present as carbonyl groups (C=O). The O1s XPS results showed that there were no significant changes in O configuration with increasing pyrolysis temperature (Table S3).

The fitting results for N species in the NCs-900-t and NCs-*T** supports are shown in Fig. S8 and Table S4. For NCs-900-t, water-steam was introduced into the pyrolysis process for a given time at 900 °C, which could effectively regulate the amount and type of N by etching carbon atoms to form CO_x due to the different water affinities of N adjacent to C species [67]. The etching process was also explored by XPS (Fig. S9 and Table S3). The C 1s XPS spectra all showed a dominant peak belonged to sp^2 hybridized carbon structure at 284.6 ± 0.1 eV which indicated the water-steam treatment had not destroyed the C structure (Fig. S9a) [59,64]. The O 1s XPS spectra proved the concentration of doubly bonded O atom increased with prolonging the water treatment time. The tendency showed the introduction of water promoted oxidation

process of the carbon in support surface to form CO_x. The N1 concentration in NCs-900-2 h and NCs-900-3 h decreased rapidly in comparison with that in NCs-900, while the concentration of N3 species increased substantially. It is worth noting that the concentration of N2 species slowly increased. The results of these N species changes are not exactly the same as those reported in the literature [67], which might contribute to the difference in the steam treatment time. For NCs-*T**, the total N content was lower than the corresponding NCs-*T* (Table 2 and S2). The N 1s XPS results indicated that the N1 concentration declined and the N3 concentration increased. The graphitic N atoms facilitated electron transfer from the NC support to the metal sites [68–70]. Additionally, the N2 concentration in NCs-*T* and NCs-*T** was similar, except the N2 concentration in NCs-900* was approximately 6% higher than that in NCs-900. The experimental results demonstrated that the N content and type could be regulated by controlling the steam treatment time and the ligand in the ZIF.

The yield of DMC was plotted against the concentration of the different N types in Fig. S10. The yield of DMC was negatively related to the N1 concentration and positively correlated with the concentrations of N2 and N3, indicating that the N2 and N3 species are active N sites on the surface of NC supports for the oxy-carbonylation of methanol to DMC. The effect of N3 species on the catalytic activity was in accordance with the results reported by Li and Ren et al. [20] using the N-doped hollow carbon sphere encapsulated Cu catalyst for the same oxy-carbonylation of methanol to DMC in a stainless-steel autoclave. However, the relationship between methanol conversion and N1 concentration was inconsistent with that reported in the literature [20,71]. Thus, much more analysis and characterizations are needed to investigate the role of different N types.

There is some scattering for the relationship between the three N types and DMC yield as shown in Fig. S10. The scattering was much larger for N3 than for the N1 and N2 species. These observations suggest that the N1 and N2 species are more closely related to the active sites for the oxy-carbonylation reaction. Because of the deviation of N1 and N2 species in the plot, further efforts were devoted to construct a better relationship between the concentration of N1 and N2 species and the catalyst activity. Cu/NCs−P-900 and Cu/NCs−P-1000 were prepared and tested for the oxy-carbonylation of methanol as comparisons with Cu/NCs-*T* and Cu/NCs-*T** because of the presence of abundant N2 species on the surface of NCs−P-*T* in Fig. S11. As for the relationship between the DMC yields over Cu-based catalysts on different NC supports as a function of N2/N1 molar ratio (Fig. 6), we can see that the catalytic performance first increased in the range of N2/N1 from 0.6 to 3.1 and then decreased when the ratio of N2/N1 increased to above 4.0. Combined with the corresponding N content, we can obtain that the NCs with an N content of 2−5 wt% and N2/N1 molar ratio of 2−3 are vital for the Cu catalysts to show a performance enhancement.

3.4. Investigation of the interaction between Cu species and NCs

The H_2−TPR characterization can provide powerful information on the interaction between metal and supports. Fig. 7 shows the H_2−TPR profiles of Cu/XC72, Cu/NCs-*T* and the corresponding supports. There are two reduction peaks for Cu/XC72 in the temperature range of 130−280 °C and 280−430 °C, which are assigned to the reduction of highly dispersed and bulk $Cu^{\delta+}$ species, respectively. The peak centered at approximately 500−750 °C is attributed to the reduction of functional groups on the XC72 surface. As for the Cu/NCs-*T* with different N contents, the primary reduction peak at 280−430 °C evidently splits into two peaks and the reduction peaks of Cu species shifted towards higher temperature due to the introduction of N species, indicating the interaction
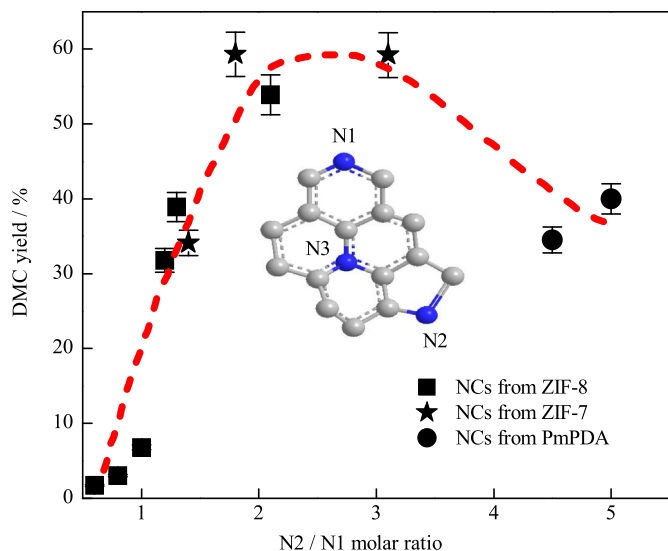
Fig. 6. Plot of DMC yield against the molar ratio of N2/N1 in NCs-*T* supports. (A colour version of this figure can be viewed online.)
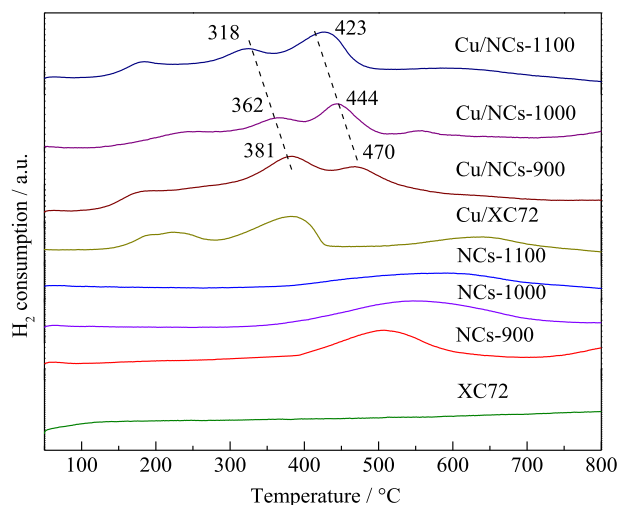
Fig. 7. H_2–TPR profiles of Cu/XC72, Cu/NCs-*T* catalysts and the corresponding supports. (A colour version of this figure can be viewed online.)

existed between the Cu and N species. The split reduction peaks for Cu/NCs-1100, Cu/NCs-1000 and Cu/NCs-900 gradually shifted at higher temperatures with increasing N content from 2.0 to 9.8 (Table 2). This shift suggests that the more N content in the supports, the stronger the interaction between Cu and N species [72,73].

It is important to know that the interfacial interaction of the Cu and N groups in the NCs plays a critical role in the valence of Cu species, which is closely related to the catalytic performance. The Cu 2p XPS measurements were performed to gain the information of Cu valence on the catalysts with different N contents and the results are displayed in Fig. S12 and Table S5. The Cu $2p_{3/2}$ spectra were fitted to two peaks at 934.6 ± 0.3 eV and 932.8 ± 0.3 eV, which were assigned to Cu^{2+} and (Cu^0+Cu^+) species, respectively [21,74,75]. The Cu^{2+} concentration in both Cu/NCs-*T* and Cu/NCs-*T** was higher than that in Cu/XC72. For Cu/NCs-900, the presence of Cu^{2+} increased to above 80% due to the presence of a high N content. The findings indicate that the interaction of Cu and N species can weaken the reduction of Cu^{2+} during the calcination process;

the higher the N content, the more difficult reduction the Cu^{2+} species. When NCs-900 was treated by water-steam for 3 h, the obtained Cu/NCs-900-3 h catalyst contained a lower concentration of Cu^{2+} species due to the decrease of N content. Thus, a proper ratio of $(Cu^0+Cu^+)/Cu^{2+}$ coupled with 2−5 wt% N content was needed for the catalysts to show an enhanced performance.

To further investigate the relationship between the catalyst structure and catalytic performance, EIS was used to explore the electron transport process across the interface of Cu and the supports. The results are displayed in Fig. 8. The size of the semicircle diameter represents the electron transfer resistance at the interface of the samples. The larger the diameter of the semicircle, the higher the electron transfer resistance. Cu/XC72 showed a larger semicircle diameter than the series of Cu catalysts supported on NCs, indicating that the introduction of N could promote the electron transfer process [76]. Among the series of Cu-based catalysts supported on NCs, Cu/NCs-1000* exhibited the smallest electron transfer resistance, which contributed to the high graphitization of NCs-1000* [65]. This result is consistent with the XPS results. All these findings confirm that the N introduction has a great influence on the catalytic performance by altering the electron transfer and interaction of Cu and N species.

3.5. Catalytic stability

The stability of the catalysts was further examined in the oxy-carbonylation of methanol to DMC, and the results of Cu/XC72, Cu/NCs-1000 and Cu/NCs-1000* are incorporated in Fig. 9. Cu/NCs-1000 and Cu/NCs-1000* catalysts showed superior stability than Cu/XC72 because the introduction of N could anchor and stabilize Cu species by the interaction. However, after reaction in stream for 60 h, the conversion of methanol decreased by approximately 10% over the Cu/NCs-1000 and Cu/NCs-1000* catalysts. To explore the reason behind the decline in the catalytic activity, a series of characterizations were used to investigate the structure of catalyst after reaction. Taking Cu/NCs-1000 as an example, after 60 h re-action, no diffraction peaks of Cu appeared as shown in Fig. S13. This finding indicated there was no large-scale agglomeration of Cu species during the reaction and the size change of Cu species was not an important factor in the activity decline. The valence of Cu species was probed by XPS in Fig. S14 and Table S5. The concentration of Cu^{2+} in the Cu/NCs-1000 declined sharply by 18% after 60 h with the increase of low-valent Cu species (Cu^0+Cu^+) concentration. The findings suggested that the change in the Cu valence might be the main cause of the decline in catalytic activity.
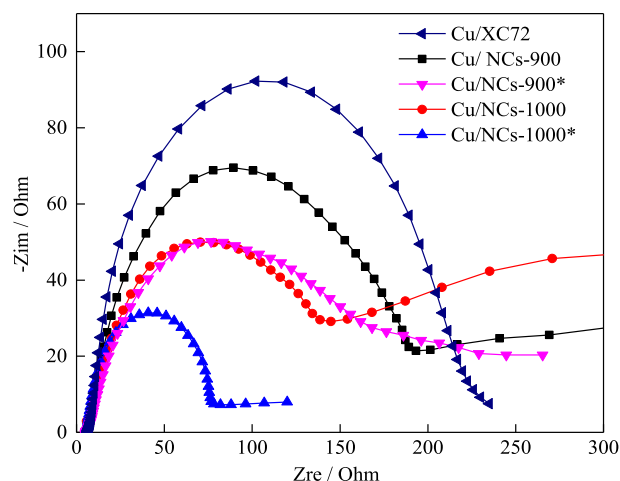
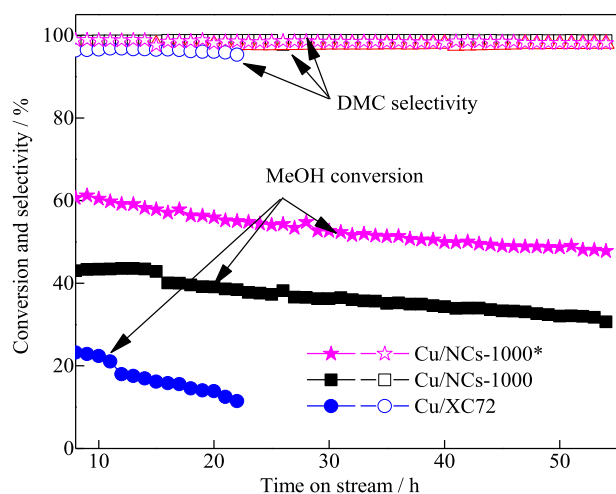**Fig. 8.** EIS plots of Cu/NCs-*T*, Cu/NCs-*T** and Cu/XC72 catalysts.

Fig. 9. Catalytic stability of Cu/NCs-1000, Cu/NCs-1000* and Cu/XC-72.

4. Conclusions

We systematically investigated the synergistic effects of N configurations on the catalysis of Cu NPs in the oxy-carbonylation of methanol to DMC. The interaction between NCs and Cu species could purposefully improve catalytic activity by tailoring the N configuration. The N type and content can be readily regulated by changing the pyrolysis atmosphere or ligand of ZIFs. The NCs with an N content of 2–5 wt% and a pyrrolic N/pyridinic N molar ratio of 2–3 endowed with Cu NPs show higher performance. The TOF of 4.4 h^{-1} over Cu NPs on pristine carbon markedly increased to 17.9 h^{-1} and 28.5 h^{-1} over Cu NPs on NCs from ZIF-8 and ZIF-7, respectively. This work constructs an efficient and stable heterogeneous Cu catalyst for the synthesis of DMC by the oxy-carbonylation of methanol with molecular oxygen and, more significantly, provides an in-depth understanding of N configuration effects on NC-supported metal nanocatalysts.

Contributions

J.Z. developed the sample synthesis approach and performed most of the experiments with X.L. W.C. and H.F. provided help in the TEM measurements. Y.Z. helped to carry out the XPS characterization. J.Z. and Y.Y. wrote the manuscript. Y.Y. guided the work. All the authors read and commented on the manuscript.

Declaration competing interest

The authors declare no competing interests.

Acknowledgments

Appendix A. Supplementary data

Supplementary data to this article can be found online at https://doi.org/10.1016/j.carbon.2019.11.064.

References

[1] H.X. Zhong, J. Wang, Y.W. Zhang, W.L. Xu, W. Xing, D. Xu, Y.F. Zhang, X.B. Zhang, ZIF-8 derived graphene-based nitrogen-doped porous carbon sheets as highly efficient and durable oxygen reduction electrocatalysts, Angew. Chem. Int. Ed. 53 (2014) 14235–14239.

[2] L. Ge, Y. Yang, L. Wang, W. Zhou, R. De Marco, Z.G. Chen, J. Zou, Z.H. Zhu, High activity electrocatalysts from metal–organic framework–carbon nanotube templates for the oxygen reduction reaction, Carbon 82 (2015) 417–424.

[3] B. Liu, H. Shioyama, H.L. Jiang, X.B. Zhang, Q. Xu, Metal–organic framework (MOF) as a template for syntheses of nanoporous carbons as electrode materials for supercapacitor, Carbon 48 (2010) 456–463.

[4] L.J. Zhang, Z.X. Su, F.L. Jiang, L.L. Yang, J.J. Qian, Y.F. Zhou, W.M. Li, M.C. Hong, Highly graphitized nitrogen-doped porous carbon nanopolyhedra derived from ZIF-8 nanocrystals as efficient electrocatalysts for oxygen reduction reactions, Nanoscale 6 (2014) 6590–6602.

[5] M. Du, K. Rui, Y.Q. Chang, Y. Zhang, Z.Y. Ma, W.P. Sun, Q.Y. Yan, J.X. Zhu, W. Huang, Carbon necklace incorporated electroactive reservoir constructing flexible papers for advanced lithium-ion batteries, Small 14 (2018) 1702770.

[6] P.C. Shi, J.D. Yi, T.T. Liu, L. Li, L.J. Zhang, C.F. Sun, Y.B. Wang, Y.B. Huang, R. Cao, Hierarchically porous nitrogen-doped carbon nanotubes derived from core–shell ZnO@zeolitic imidazolate framework nanorods for highly efficient oxygen reduction reactions, J. Mater. Chem. A 5 (2017) 12322–12329.

[7] X. Niu, L. Wan, Z. Hou, T.Y. Wang, C.S. Sun, J. Sun, P. Zhao, T.Y. Jiang, S.L. Wang, Mesoporous carbon as a novel drug carrier of fenofibrate for enhancement of the dissolution and oral bioavailability, Int. J. Pharm. 452 (2013) 382–389.

[8] Q.F. Zhao, Y.Z. Lin, N. Han, X. Li, H.J. Geng, X.D. Wang, Y. Cui, S.L. Wang, Mesoporous carbon nanomaterials in drug delivery and biomedical application, Drug Deliv. 24 (2017) 94–107.

[9] Y. Liu, C. Wu, Y.N. Hao, J. Xu, Y. Zhao, Y. Qiu, J. Jiang, T. Yu, P. Ji, Preparation of a novel starch-derived three-dimensional ordered macroporous carbon for improving the dissolution rate and oral bioavailability of water-insoluble drugs, J. Pharm. Biomed. Anal. 118 (2016) 267–275.

[10] Y.J. Wang, A.D. Price, F. Caruso, Nanoporous colloids: building blocks for a new generation of structured materials, J. Mater. Chem. 19 (2009) 6451–6464.

[11] R. Li, X.Q. Ren, X. Feng, X.G. Li, C.W. Hu, B. Wang, A highly stable metal- and nitrogen-doped nanocomposite derived from Zn/Ni-ZIF-8 capable of CO_2 capture and separation, Chem. Commun. 50 (2014) 6894–6897.

[12] Y. Yang, L. Ge, V. Rudolph, Z.H. Zhu, In situ synthesis of zeolitic imidazolate frameworks/carbon nanotube composites with enhanced CO_2 adsorption, Dalton Trans. 43 (2014) 7028–7036.

[13] H.L. Jiang, B. Liu, Y.Q. Lan, K. Kuratani, T. Akita, H. Shioyama, F. Zong, Q. Xu, From metal-organic framework to nanoporous carbon: toward a very high surface area and hydrogen uptake, J. Am. Chem. Soc. 133 (2011) 11854–11857.

[14] Y. Gong, X. Zhao, H. Zhang, B. Yang, K. Xiao, T. Guo, J.J. Zhang, H.X. Shao, Y.B. Wang, G. Yu, MOF-derived nitrogen doped carbon modified g-C_3N_4 heterostructure composite with enhanced photocatalytic activity for bisphenol A degradation with peroxymonosulfate under visible light irradiation, Appl. Catal. B Environ. 233 (2018) 35–45.

[15] K. Shen, X.D. Chen, J.Y. Chen, Y.W. Li, Development of MOF-derived carbon-based nanomaterials for efficient catalysis, ACS Catal. 6 (2016) 5887–5903.

[16] H. Watanabe, S. Asano, S. Fujita, H. Yoshida, M. Arai, Nitrogen-doped, metal-free activated carbon catalysts for aerobic oxidation of alcohols, ACS Catal. 5 (2015) 2886–2894.

[17] X. Cui, Y. Li, S. Bachmann, M. Scalone, A.E. Surkus, K. Junge, C. Topf, M. Beller, Synthesis and characterization of iron-nitrogen-doped graphene/core-shell catalysts: efficient oxidative dehydrogenation of n-heterocycles, J. Am. Chem. Soc. 137 (2015) 10652–10658.

[18] J.P. Zhang, S. Nagamatsu, J.M. Du, C.L. Tong, H.H. Fang, D.H. Deng, K. Asakura, Y.Z. Yuan, A study of FeN$_X$/C catalysts for the selective oxidation of unsaturated alcohols by molecular oxygen, J. Catal. 367 (2018) 16–26.

[19] R.F. Nie, H.H. Yang, H.F. Zhang, X.L. Yu, X.H. Lu, D. Zhou, Q.H. Xia, Mild-temperature hydrodeoxygenation of vanillin over porous nitrogen-doped carbon black supported nickel nanoparticles, Green Chem. 19 (2017) 3126–3134.

[20] H.X. Li, J.X. Zhao, R.N. Shi, P.P. Hao, S.S. Liu, Z. Li, J. Ren, Remarkable activity of nitrogen-doped hollow carbon spheres encapsulated Cu on synthesis of dimethyl carbonate: role of effective nitrogen, Appl. Surf. Sci. 436 (2018) 803–813.

[21] R.N. Shi, J.X. Zhao, S.S. Liu, W. Sun, H.X. Li, P.P. Hao, Z. Li, J. Ren, Nitrogen-doped graphene supported copper catalysts for methanol oxidative carbonylation: enhancement of catalytic activity and stability by nitrogen species, Carbon 130 (2018) 185–195.

[22] G.Q. Zhang, Z. Li, H.Y. Zheng, T.J. Fu, Y.B. Ju, Y.C. Wang, Influence of the surface oxygenated groups of activated carbon on preparation of a nano Cu/AC catalyst and heterogeneous catalysis in the oxidative carbonylation of methanol, Appl. Catal. B Environ. 179 (2015) 95–105.

[23] T.J. Fu, X. Wang, H.Y. Zheng, Z. Li, Effect of Cu location and dispersion on carbon sphere supported Cu catalysts for oxidative carbonylation of methanol to dimethyl carbonate, Carbon 115 (2017) 363–374.

[24] X.P. Shi, H.B. Yu, S. Gao, X.Y. Li, H.H. Fang, R.J. Li, Y.Y. Li, L.J. Zhang, X.L. Liang, Y.Z. Yuan, Synergistic effect of nitrogen-doped carbon-nanotube-supported Cu–Fe catalyst for the synthesis of higher alcohols from syngas, Fuel 210 (2017) 241–248.

[25] Y.Z. Chen, G.R. Cai, Y.M. Wang, Q. Xu, S.H. Yua, H.L. Jiang, Palladium

nanoparticles stabilized with N-doped porous carbons derived from metal−organic frameworks for selective catalysis in biofuel upgrade_ the role of catalyst wettability, Green Chem. 18 (2016) 1212−1217.

[26] Y. Cao, S. Mao, M. Li, Y. Chen, Y. Wang, Metal/porous carbon composites for heterogeneous catalysis: old catalysts with improved performance promoted by N-doping, ACS Catal. 7 (2017) 8090−8112.

[27] L.T. Qu, Y. Liu, J.B. Baek, L.M. Dai, Nitrogen-doped graphene as efficient metal-free electrocatalyst for oxygen reduction in fuel cells, ACS Nano 4 (2010) 1321−1326.

[28] Z. Jin, J. Yao, C. Kittrell, J.M. Tour, Large-scale growth and characterizations of nitrogen-doped monolayer graphene sheets, ACS Nano 5 (2011) 4112−4117.

[29] Z.C. Ying, R.L. Hettich, R.N. Compton, R.E. Haufler, Synthesis of nitrogen doped fullerenes by laser ablation, J. Phys. B-At. Mol. Opt. 29 (1996) 4935−4942.

[30] N. Menegazzo, M. Kahn, R. Berghauser, W. Waldhauser, B. Mizaikoff, Nitrogen doped diamond-like carbon as optically transparent electrode for infrared attenuated total reflection spectroelectrochemistry, Analyst 136 (2011) 1831−1839.

[31] S. Liu, J.S. Zhou, H.H. Song, Tailoring highly N-doped carbon materials from hexamine-based MOFs: superior performance and new insight into the roles of N configurations in Na-ion storage, Small 14 (2018) 1703548.

[32] G. Wu, K.L. More, C.M. Johnston, P. Zelenay, High performance lectrocatalysts for oxygen reduction derived from polyaniline, iron, and cobalt, Science 332 (2011) 443−447.

[33] D.H. Guo, R. Shibuya, C. Akiba, S. Saji, T. Kondo, J. Nakamura, Active sites of nitrogen-doped carbon materials for oxygen reduction reaction clarified using model catalysts, Science 351 (2016) 361−365.

[34] X.M. Ning, Y.H. Li, J.Y. Ming, Q. Wang, H.J. Wang, Y.H. Cao, F. Peng, Y.H. Yang, H. Yu, Electronic synergism of pyridinic- and graphitic-nitrogen on N-doped carbons for the oxygen reduction reaction, Chem. Sci. 10 (2019) 1589−1596.

[35] G. Zhang, D. Zhao, J. Yan, D. Jia, H. Zheng, J. Mi, Z. Li, The promotion and stabilization effects of surface nitrogen containing groups of CNT on cu-based nanoparticles in the oxidative carbonylation reaction, Appl. Catal. Gen. 579 (2019) 18−29.

[36] W.B. Gong, Y. Lin, C. Chen, M. Al-Mamun, H.S. Lu, G.Z. Wang, H.M. Zhang, H.J. Zhao, Nitrogen-doped carbon nanotube confined Co-N_x Sites for selective hydrogenation of biomass-derived compounds, Adv. Mater. (2019), e1808341.

[37] H.Y. Niu, S.L. Liu, Y.Q. Cai, F.C. Wu, X.L. Zhao, MOF derived porous carbon supported Cu/Cu_2O composite as high performance non-noble catalyst, Microporous Mesoporous Mater. 219 (2016) 48−53.

[38] L.N. Chong, J.G. Wen, J. Kubal, F.G. Sen, J.X. Zou, J. Greeley, M. Chan, H. Barkholtz, W.J. Ding, D.J. Liu, Ultralow-loading platinum-cobalt fuel cell catalysts derived from imidazolate frameworks, Science 362 (2018) 1276−1281.

[39] R.V. Jagadeesh, K. Murugesan, A.S. Alshammari, H. Neumann, M.M. Pohl, J. Radnik, M. Beller, MOF-derived cobalt nanoparticles catalyze a general synthesis of amines, Science 358 (2017) 326−332.

[40] B. An, K. Cheng, C. Wang, Y. Wang, W.B. Lin, Pyrolysis of metal−organic frameworks to Fe_3O_4@Fe_5C_2 core−shell nanoparticles for Fischer−Tropsch synthesis, ACS Catal. 6 (2016) 3610−3618.

[41] B. Liu, H. Shioyama, T. Akita, Q. Xu, Metal-organic framework as a template for porous carbon, J. Am. Chem. Soc. 130 (2008) 5390−5391.

[42] N.L. Torad, R.R. Salunkhe, Y. Li, H. Hamoudi, M. Imura, Y. Sakka, C.C. Hu, Y. Yamauchi, Electric double-layer capacitors based on highly graphitized nanoporous carbons derived from ZIF-67, Chem. Eur J. 20 (2014) 7895−7900.

[43] K.S. Park, Z. Ni, A.P. Cote, J.Y. Choi, R. Huang, F.J. Uribe-Romo, H.K. Chae, M. O'Keeffe, O.M. Yaghi, Exceptional chemical and thermal stability of zeolitic imidazolate frameworks, Proc. Natl. Acad. Sci. U.S.A. 103 (2006) 10186−10191.

[44] S. Ma, G.A. Goenaga, A.V. Call, D.J. Liu, Cobalt imidazolate framework as precursor for oxygen reduction reaction electrocatalysts, Chem. Eur J. 17 (2011) 2063−2067.

[45] Y. Li, L.L. Zhao, Z.L. Du, J. Du, W. Wang, Y. Wang, L.J. Zhao, X.M. Cao, X.H. Zhong, Metal−organic framework derived Co,N-bidoped carbons as superior electrode catalysts for quantum dot sensitized solar cells, J. Mater. Chem. A 6 (2018) 2129−2138.

[46] P. Zhang, F. Sun, Z. Xiang, Z. Shen, J. Yun, D. Cao, ZIF-derived in situ nitrogen-doped porous carbons as efficient metal-free electrocatalysts for oxygen reduction reaction, Energy Environ. Sci. 7 (2014) 442−450.

[47] W. Chaikittisilp, M. Hu, H. Wang, H.S. Huang, T. Fujita, K.C. Wu, L.C. Chen, Y. Yamauchi, K. Ariga, Nanoporous carbons through direct carbonization of a zeolitic imidazolate framework for supercapacitor electrodes, Chem. Commun. 48 (2012) 7259−7261.

[48] L.J. Li, J.X. He, Y. Wang, X.X. Lv, X. Gu, P.C. Dai, D.D. Liu, X.B. Zhao, Metal−organic frameworks: a promising platform for constructing non-noble electrocatalysts for the oxygen-reduction reaction, J. Mater. Chem. A 7 (2019) 1964−1988.

[49] Q. Li, J. Guo, H. Zhu, F. Yan, Space confined synthesis of ZIF-67 nanoparticles in hollow carbon nanospheres for CO_2 adsorption, Small 15 (2019) 1804874.

[50] Y.H. Li, X.H. Cai, S.J. Chen, H. Zhang, K.H.L. Zhang, J.Q. Hong, B.H. Chen, D.H. Kuo, W.J. Wang, Highly dispersed metal carbide on ZIF-derived pyridinic-N-doped carbon for CO_2 enrichment and selective hydrogenation, ChemSusChem 11 (2018) 1040−1047.

[51] C. Srinivas, M. Sudharsan, G.R.K. Reddy, P.S. Kumar, A.J. Amali, D. Suresh, Co/Co-N@nanoporous carbon derived from ZIF-67: a highly sensitive and selective electrochemical dopamine sensor, Electroanalysis 30 (2018) 2475−2482.

[52] J. Yang, F. Zhang, H. Lu, X. Hong, H. Jiang, Y. Wu, Y. Li, Hollow Zn/Co ZIF particles derived from core-shell ZIF-67@ZIF-8 as selective catalyst for the semi-hydrogenation of acetylene, Angew. Chem. Int. Ed. 54 (2015) 10889−10893.

[53] C.M. Zhao, X.Y. Dai, T. Yao, W.X. Chen, X.Q. Wang, J. Wang, J. Yang, S.Q. Wei, Y. Wu, Y.D. Li, Ionic exchange of metal-organic frameworks to access single nickel sites for efficient electroreduction of CO_2, J. Am. Chem. Soc. 139 (2017) 8078−8081.

[54] S. Lee, J. Kim, J. Kim, D. Lee, Zeolitic imidazolate framework membrane with marked thermochemical stability for high-temperature catalytic processes, Chem. Mater. 30 (2018) 447−455.

[55] X. Wang, Y.W. Li, Nanoporous carbons derived from MOFs as metal-free catalysts for selective aerobic oxidations, J. Mater. Chem. A 4 (2016) 5247−5257.

[56] D.Y. Qu, Investigation of hydrogen physisorption active sites on the surface of porous carbonaceous materials, Chem. Eur J. 14 (2008) 1040−1046.

[57] Y.H. Liu, J.S. Xue, T. Zheng, J.R. Dahn, Mechanism of lithium insertion in hard carbons prepared by pyrolysis of epoxy resins, Carbon 34 (1996) 193−200.

[58] S. Liu, Z. Wang, S. Zhou, F. Yu, M. Yu, C.Y. Chiang, W. Zhou, J. Zhao, J. Qiu, Metal−organic−framework−derived hybrid carbon nanocages as a bifunctional electrocatalyst for oxygen reduction and evolution, Adv. Mater. 29 (2017) 1700874.

[59] B.Y. Xia, Y. Yan, N. Li, H.B. Wu, X.W. Lou, X. Wang, A metal−organic framework-derived bifunctional oxygen electrocatalyst, Nat. Energy 1 (2016), https://doi.org/10.1038/nenergy.2015.6.

[60] J. Cravillon, R. Nayuk, S. Springer, A. Feldhoff, K. Huber, M. Wiebcke, Controlling zeolitic imidazolate framework nano- and microcrystal formation: insight into crystal growth by time-resolved in situ static light scattering, Chem. Mater. 23 (2011) 2130−2141.

[61] X.G. Han, L.M. Sun, F. Wang, D. Sun, MOF-derived honeycomb-like N-doped carbon structures assembled from mesoporous nanosheets with superior performance in lithium-ion batteries, J. Mater. Chem. A 6 (2018) 18891−18897.

[62] S.I. Fujita, K. Yamada, A. Katagiri, H. Watanabe, H. Yoshida, M. Arai, Nitrogen-doped metal-free carbon catalysts for aerobic oxidation of xanthene, Appl. Catal. Gen. 488 (2014) 171−175.

[63] J.R. Pels, F. Kapteijn, J.A. Moulijn, Q. Zhu, K.M. Thomas, Evolution of nitrogen functionalities in carbonaceous materials during pyrolysis, Carbon 33 (1995) 1641−1653.

[64] M. Chandran, M. Shasha, S. Michaelson, A. Hoffman, Incorporation of low energy activated nitrogen onto Hopg surface: chemical states and thermal stability studies by in-situ XPS and Raman spectroscopy, Appl. Surf. Sci. 382 (2016) 192−201.

[65] Y.Z. Chen, C. Wang, Z.Y. Wu, Y. Xiong, Q. Xu, S.H. Yu, H.L. Jiang, From bimetallic metal-organic framework to porous carbon: high surface area and multi-component active dopants for excellent electrocatalysis, Adv. Mater. 27 (2015) 5010−5016.

[66] D.J. Mowbray, A.P. Paz, G. Ruiz-Soria, M. Sauer, P. Lacovig, M. Dalmiglio, S. Lizzit, K. Yanagi, A. Goldoni, T. Pichler, P. Ayala, A. Rubio, Disentangling vacancy oxidation on metallicity-sorted carbon nanotubes, J. Phys. Chem. C 120 (2016) 18316−18322.

[67] X.Q. Cui, Z.Y. Pan, L.J. Zhang, H.S. Peng, G.F. Zheng, Selective etching of nitrogen-doped carbon by steam for enhanced electrochemical CO_2 reduction, Adv. Energy Mater. 7 (2017) 1701456.

[68] J.L. Long, K. Shen, L. Chen, Y.W. Li, Multimetal-MOF-derived transition metal alloy NPs embedded in an N-doped carbon matrix: highly active catalysts for hydrogenation reactions, J. Mater. Chem. A 4 (2016) 10254−10262.

[69] L.F. Lai, J.R. Potts, D. Zhan, L. Wang, C.K. Poh, C.H. Tang, H. Gong, Z.X. Shen, J.Y. Lin, R.S. Ruoff, Exploration of the active center structure of nitrogen-doped graphene-based catalysts for oxygen reduction reaction, Energy Environ. Sci. 5 (2012) 7936−7942.

[70] P. Wang, Z.K. Wang, L.X. Jia, Z.L. Xiao, Origin of the catalytic activity of graphite nitride for the electrochemical reduction of oxygen: geometric factors vs. electronic factors, Phys. Chem. Chem. Phys. 11 (2009) 2730−2740.

[71] X.X. Han, W. Sun, C.F. Zhao, R.N. Shi, X.H. Wang, S.S. Liu, Z. Li, J. Ren, Synthesis of dimethyl carbonate on single Cu atom embedded in N-doped graphene: effect of nitrogen species, Mol. Catal. 443 (2017) 1−13.

[72] R.F. Zhou, S.Z. Qiao, Silver/nitrogen-doped graphene interaction and its effect on electrocatalytic oxygen reduction, Chem. Mater. 26 (2014) 5868−5873.

[73] A. Zamudio, A.L. Elias, J.A. Rodriguez-Manzo, F. Lopez-Urias, G. Rodriguez-Gattorno, F. Lupo, M. Ruhle, D.J. Smith, H. Terrones, D. Diaz, M. Terrones, Efficient anchoring of silver nanoparticles on N-doped carbon nanotubes, Small 2 (2006) 346−350.

[74] L. Xu, L. Yang, Z.W. Hu, S.H. Yu, Comparison study on the stability of copper nanowires and their oxidation kinetics in gas and liquid, ACS Nano 10 (2016) 3823−3834.

[75] F.L. Meng, H.X. Zhong, Q. Zhang, K.H. Liu, J.M. Yan, Q. Jiang, Integrated Cu_3N porous nanowire array electrode for high-performance supercapacitors, J. Mater. Chem. A 5 (2017) 18972−18976.

[76] N.S. Anuar, W.J. Basirun, M. Ladan, M. Shalauddin, M.S. Mehmood, Fabrication of platinum nitrogen-doped graphene nanocomposite modified electrode for the electrochemical detection of acetaminophen, Sens. Actuators B Chem. 266 (2018) 375−383.